An Innovative Data Processing Method for Studying Nanoparticle Formation in Droplet Microfluidics using X-rays Scattering

Dimitri Radajewski*[a], Liam Hunter[a], Xuefeng He[a], Ouassef Nahi[a], Johanna M. Galloway[a] and Fiona C. Meldrum*[a]

X-ray scattering techniques provide a powerful means of characterizing the formation of nanoparticles in solution. Coupling these techniques to segmented-flow microfluidic devices that offer well-defined environments gives access to in situ time-resolved analysis, excellent reproducibility, and eliminates potential radiation damage. However, analysis of the resulting datasets can be extremely time-consuming, where these comprise frames corresponding to the droplets alone, the continuous phase alone, and to both at their interface. We here describe a robust, low-cost, and versatile droplet microfluidics device and use it to study the formation of magnetite nanoparticles with simultaneous synchrotron SAXS and WAXS. Lateral outlet capillaries facilitate the X-ray analysis and reaction times of between a few seconds and minutes can be accommodated. A two-step data processing method is then described that exploits the unique WAXS signatures of the droplets, continuous phase, and interfacial region to identify the frames corresponding to the droplets. These are then sorted, and the background scattering is subtracted using an automated frame-by-frame approach, allowing the signal from the nanoparticles to be isolated from the raw data. Modeling these data gives quantitative information about the evolution of the sizes and structures of the nanoparticles, in agreement with TEM observations. This versatile platform can be readily employed to study a wide range of dynamic processes in heterogeneous systems.

1. Introduction

X-ray scattering techniques are used extensively to investigate the structures of hard and soft matter systems.[1–3] Small Angle X-ray Scattering (SAXS) can provide information including molecular interactions[4] and weights,[5] structural conformations,[6,7] the folding dynamics of proteins in solution,[8] and the formation of nanoparticles[9], while Wide Angle X-ray Scattering (WAXS) reveals the crystal structures of both organic and inorganic materials. Simultaneous SAXS/WAXS provides a particularly powerful means of studying dynamic processes such as nanoparticle nucleation and growth.[10–17] Many of these applications require that large parameter spaces are screened, that analyses are conducted with small quantities of sample, and that data is recorded at short time-scales with excellent time resolution. Microfluidic devices provide an attractive means of meeting these demands, and their small sizes make them well-suited to the sample environments available at many synchrotron beamlines. The continuous flow through these devices also constantly renews the sample such that radiation damage that can arise from extended exposure to high energy X-rays is virtually eliminated.[18]

A range of microfluidic devices have been constructed to facilitate on-chip X-ray analysis.[19] The simplest designs allow mixing of reagents, and analysis is conducted by focusing the beam on an X-ray transparent capillary positioned at the exit of the device.[20,21] Chips can also be constructed with microfluidics channels sealed with X-ray transparent films such as Kapton or Mylar, creating an observation window.[22,23] Different positions along the channels correspond to different reaction times, thereby facilitating time-resolved investigations. Such devices have been operated with continuous flows to study dynamic processes such as protein folding,[24] the behavior of lipidic mesophases[25] and the assembly of surfactants[26] and intermediate filaments,[27] as well as the nucleation and growth of inorganic

nanoparticles.[28292230] However, continuous flow systems often suffer from clogging, where this can be particularly significant in crystallization processes.[31] This can be avoided using segmented-flow microfluidic systems in which the droplets behave as independent microreactors and the continuous phase lubricates the microchannels, reducing the likelihood of clogging. With the creation of numerous, identical droplets these systems also deliver statistically reliable data.[32]

These multiphasic systems have been used to screen conditions for crystallizing proteins,[33,34] to measure nucleation kinetics of organic molecules[35,36] and inorganic salts,[37,38] and to synthesize inorganic nanoparticles.[39–42] Combining droplet-based microfluidics with X-ray analysis remains challenging, however, due in part to the complexity of extracting data from flowing droplets. During analysis, the X-ray detector collects frames at a rate that exceeds the frequency of passing droplets such that frames are collected from the aqueous droplets, the continuous oil phase, and the interface between these. Two fundamentally different approaches can be used to create datasets corresponding to the droplets alone, where selection is achieved either (i) at the point of data collection or (ii) after. The former is conducted using on-line image analysis to detect droplets close to the beam position, which triggers the shutter to open and data acquisition to begin. Frames are only collected from the droplets and all can be used in the analysis. This method has been used to study protein structures and interactions using SAXS.[20,21] The second method is experimentally straightforward, but then requires the droplet frames to be isolated. This can be achieved by identifying characteristic features in the frames. This technique has been used to investigate the crystallization of calcium carbonate in flowing droplets using WAXS.[23] Droplet microfluidics and SAXS have also been combined to investigate the formation of liquid

crystal[43] and gold nanoparticles[9] but the methods used to process the data were not described in detail.

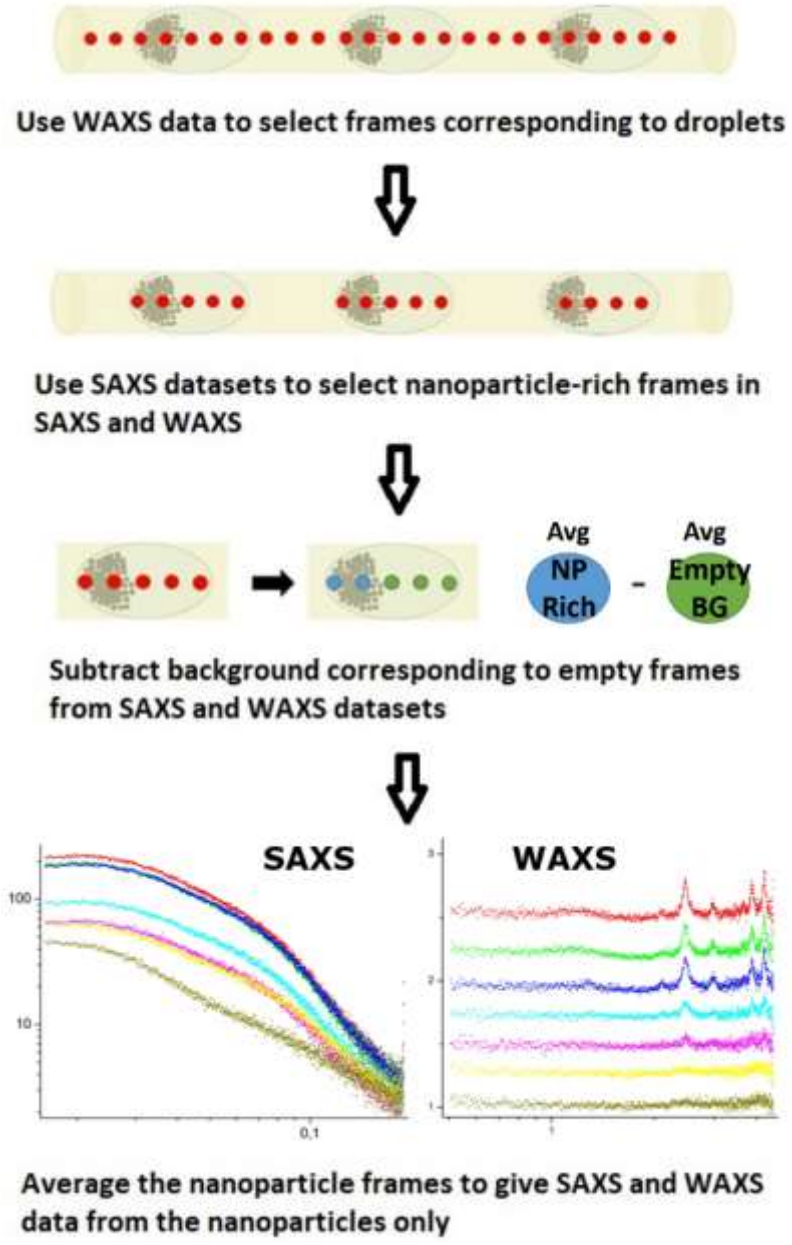

Figure 1. Summary of the two-step data processing technique based on simultaneous SAXS and WAXS acquisition from droplets flowing through a capillary.

In this work, a two-steps data processing technique based on simultaneous SAXS and WAXS acquisition from droplets is used and summarized in Figure 1. Data are recorded as a continuous sequence of snapshots. Features present in the WAXS patterns allow the

unwanted oil and interface frames to be discarded, and the SAXS frames then allow those from the droplets to be sorted between nanoparticle-rich and solution-only frames. Subsequent frame-to-frame subtraction gives data from the nanoparticles alone.

2. Materials and Methods

2.1 Magnetite Synthesis

Magnetite (Fe_3O_4) is a mixed-valence ($Fe(II)Fe(III)_2O_4$) magnetic iron oxide with an inverse spinel structure whose ferromagnetic properties are used in many technological applications[44,45]. It also occurs in geology and as a biomineral,[46] and is used in organisms such as bacteria for magnetotaxis.[47] In the current experiments, magnetite nanoparticles were synthesized using a co-precipitation method.[48,49] It is noted that small magnetite nanoparticles rapidly oxidize to maghemite (γ-Fe_2O_3) and that magnetite and maghemite are indistinguishable by electron diffraction[50]. We can therefore not conclusively state whether the particles synthesized were magnetite or maghemite. A solution containing Fe^{2+} and Fe^{3+} precursors was mixed with sodium hydroxide solution at room temperature, according to the following equation:

$$2\,Fe^{3+} + Fe^{2+} + 8\,OH^- \rightarrow Fe_3O_4 + H_2O \qquad \text{Eq.1}$$

Coprecipitation is cheap and experimentally straightforward, and flow systems have been explored to achieve greater control over the product nanoparticles.[51] The potential of using segmented-flow microfluidic devices has also been investigated, where Frenz et al. initiated intra-droplet precipitation by merging pairs of droplets carrying Fe(II)/Fe(III) and NH_4OH.[52]

Stock solutions of 100 mM iron(II), 100 mM iron(III), and 1M NaOH were prepared by dissolving the corresponding solids ($FeCl_3.7H_2O$, $FeCl_2.4H_2O$, NaOH, Sigma-Aldrich) in anoxic Milli-Q water that was deoxygenated by sparging with N_2 for at least 2 hours, and a stream of N_2 was bubbled through all solutions once made up to minimize areal oxidation. Preliminary experiments in bulk solution were performed to identify suitable reaction conditions for the *on-chip* synthesis and showed that magnetite formed within 2 mins on combining the stock solutions with water under continuous stirring to give concentrations of $[Fe^{2+}] = [Fe^{3+}] = 25$ mM and [NaOH] = 250 mM. The resulting nanoparticles were black and were attracted to a magnet. Nanoparticles were collected on a Transmission Electron Microscopy (TEM) grid (formvar and carbon-coated copper 200 mesh, EMS, USA) and were imaged on a FEI Tecnai TF20 FEGTEM at 200 keV using a Gatan Orius SC600A CCD camera. Selected Area Electron Diffraction (SAED) was fitted using AMCSD file #7766 for magnetite. Image analysis was performed with the software ImageJ to determine the sizes of the nanoparticles from the TEM image.

2.2 Microfluidic Design

The microfluidic design used is shown in Figure 2 and comprises two parts. The first is a classic Y-junction where the Fe(II)/Fe(III) solution, the NaOH solution, and water are mixed with respective flowrates of 2, 2 and 4 µL/min, to give final concentrations of $[Fe^{2+}] = [Fe^{3+}] = 25$ mM and [NaOH] = 250mM. This aqueous stream is periodically split into droplets by an immiscible fluorinated oil (FC-40, Fluorinert, 3M) containing a biocompatible PEG-PFPE amphiphilic block copolymer that was synthesized in-house, and which stabilizes droplet generation and controls the wetting properties. The water flow positioned between the Fe(II)/Fe(III) and NaOH solutions is used to delay the contact between the iron and base

solutions. This prevents adventitious precipitation at the junction that can cause clogging and ensures that the nanoparticles only form within the droplets.

The second section of the microfluidic device is a serpentine channel of length 46 cm whose purpose is to increase the residence time of the droplets on the chip. Kapton-coated fused silica capillaries are positioned along the channel such that they lie perpendicular to the long axis of the device. These can be individually opened to divert the flow of droplets, and the X-ray beam is focused on the active capillary. Each capillary corresponds to a different reaction time, where residence times between a few seconds and a few minutes can be achieved according to the flowrates of the incoming stock solutions. Droplets were collected from the first and last capillaries and were placed on TEM grids. The grid was then washed by adding 10 µL ethanol, blotting, and adding 10 µL deoxygenated water, and blotting dry. This process was repeated twice more to eliminate the carrier oil.

2.3 Microfluidic Fabrication

Microfluidic devices with rectangular channels of cross-section 300×300 µm^2 were prepared from polydimethylsiloxane (PDMS) on a glass slide using standard soft lithography and cast moulding techniques.[53] Briefly, a permanent epoxy negative photoresist (SU-8 2100, MicroChem, USA) was spin-coated onto a silicon wafer (Inseto, UK) to give a uniform 300 µm thick resist layer. The design shown in Figure 2a was patterned on the resist by UV exposure through an emulsion mask and structures were obtained after development of the non-exposed resist. Liquid PDMS obtained from an elastomer kit (Sylgard 184, Dow Corning, USA) was poured onto the master SU-8 structure and oven-cured before being gently peeled off. The obtained PDMS stamp and a glass slide were both plasma-activated in a plasma cleaner

(Diener Electronic, Germany) before bonding to seal the microchannels. Holes for the different inlets were made in the PDMS with microfluidic biopsy punchers (Kai Medical, Japan) corresponding to the size of the tubing (ID 350µm, OD 380µm, Portex, Smiths Medical, US) used to flow the solutions from the neMESYS syringe pumps (Cetoni, Germany) to the chip. Fused-silica capillaries coated with polyimide (ID 250µm, OD 350µm, Polymicro Technologies, USA) that are known to resist X-rays and exhibit low scattering are glued with an epoxy resin to the lateral exits of the chip and direct the output droplets past the beam (Figure 2b)**Error! Reference source not found.**.

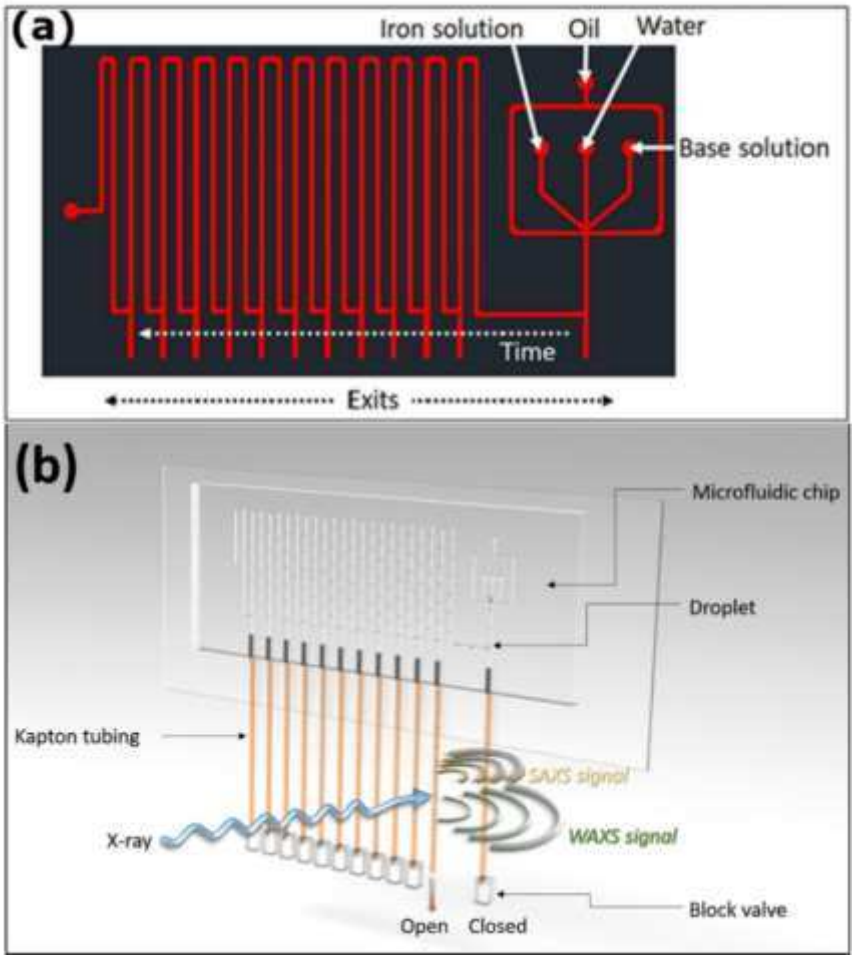

Figure 2. (a) Droplet-based microfluidic design used for the synthesis of magnetite nanoparticles. The width of the channels is 300 µm. The iron and base solutions are mixed at a Y junction and oil separates the flow into droplets. (b) Schematic of the experimental set-

up used on beamline ID22 at Diamond with the microfluidic chip positioned in a chip-holder such that the lateral capillaries are situated in front of the X-ray beam. The platform is translated horizontally such that the desired capillary is positioned in front of the beam.

2.4 Beamline Experiment Set-up

This device was used on beamline ID22 at Diamond and SAXS/WAXS patterns were recorded simultaneously. The device mounted on the beamline as shown in Figure 2b, where the exit capillaries were positioned at the same height as the beam. Horizontal translation of the device enabled the different capillaries – which correspond to different residence times – to be positioned in front of the beam. In a standard experiment, droplets were sent to the first capillary to investigate a short reaction time of 10 sec. A micro-focused X-ray beam of size 40 µm × 40 µm was employed to collect data such that it fitted within a single droplet. A dataset consisting of 1000, 20 ms snapshots was recorded for a total of 20 sec. With the flowrates mentionned before, a single droplet takes 110ms to entirely pass in front of the beam, therefore, the 20 ms acquisition time is short enough to record five snapshots from an individual droplet, and an average of 100 droplets flowed past the beam over 20 sec. Simultaneous SAXS and WAXS patterns were collected using the two beamline detectors, Pilatus P3-2M (SAXS) and Pilatus P3-2M-DLS-L (WAXS) positionned 9m and 17cm away from sample respectively. After collection of a dataset, the capillary was closed and the droplets were then sent to the second capillary which corresponds to a reaction time of 30 sec. Further horizontal translation of the platform gives access to longer reaction times.

3. Results and Discussion

3.1 TEM Characterization of Nanoparticles

TEM imaging was performed on three different samples: one from the bulk synthesis after 2 minutes and two from the microfluidic synthesis for residence times of 10 sec and 130 sec. As illustrated in

Figure 3, nanoparticles with diameters ≈ 8.3nm formed in the bulk control experiments. Analysis of the particles using selected area electron diffraction (SAED) yielded well-defined diffraction rings, patterns consistent with highly crystalline magnetite/maghemite, although their black color is consistent with magnetite. Early reaction times were accessed using the microfluidic device. Poorly crystalline particles showing only 2 weak, diffuse rings in SAED were observed after 10 sec. Well-crystalline particles with diameters of ≈ 5,4 nm were observed after a residence time of 130 sec, where the SAED intense rings, similar to those obtain with the bulk experiment were consistent with magnetite/maghemite. The sizes of the bulk and microfluidics nanoparticles are obtained from image analysis, the results are available in Supplementary Information. These data also demonstrate a phase transition from poorly crystalline material to well-crystalline particles as the reaction progresses. That the particles formed on-chip are smaller, and have a narrower size distribution than those produced in bulk solution can be attributed to better mixing in the flowing droplets. These results underline the feasibility of magnetite synthesis on-chip and the benefits of studying the crystallization process using this approach.

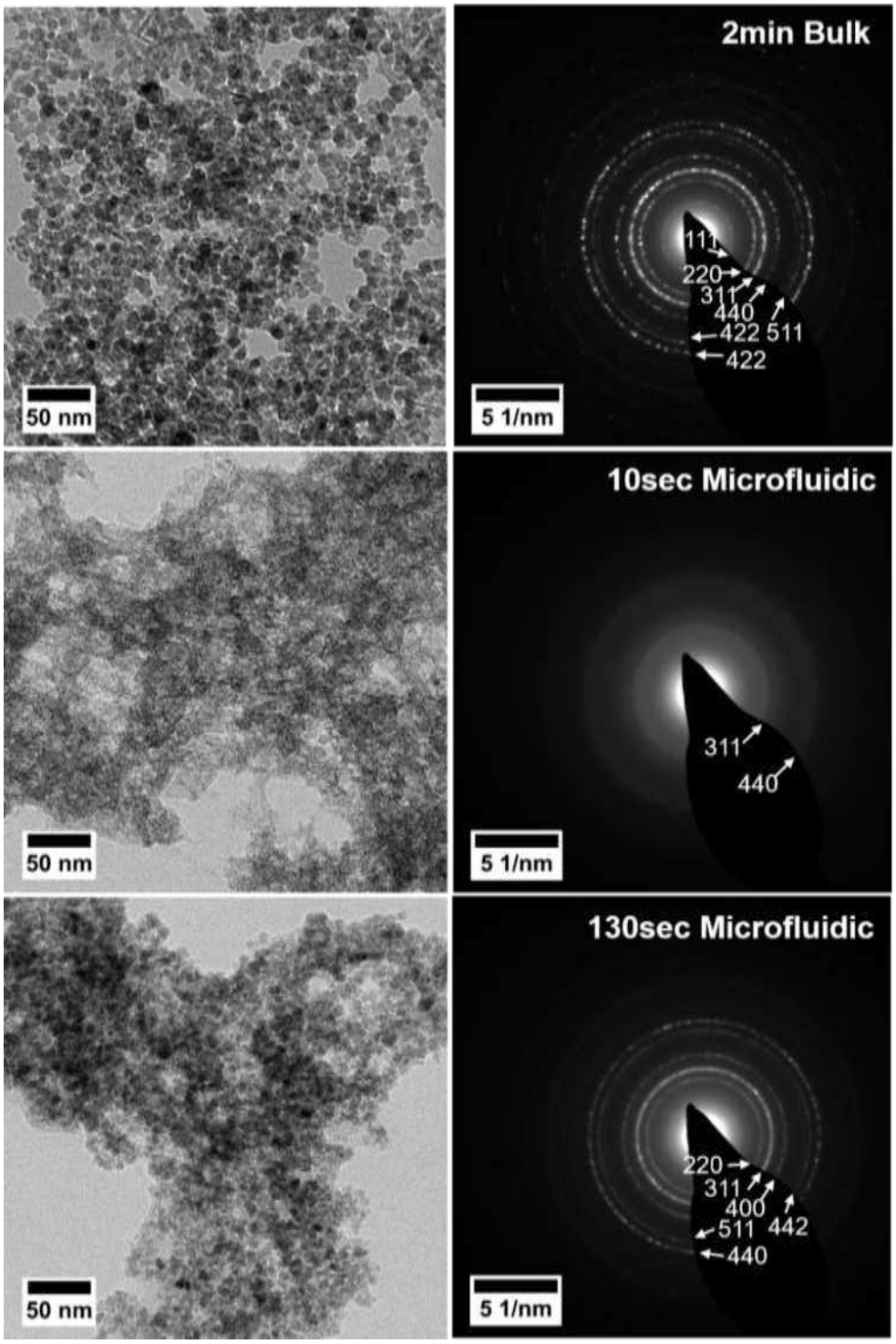

Figure 3. TEM characterization of the bulk and microfluidic synthesis. Both approaches resulted in magnetite formation with a crystallinity that increases as a function of the residence time in the microfluidic chip. The size of the nanoparticles is slightly smaller and their distribution narrower for the microfluidic synthesis.

3.2 Analysis of X-ray Scattering Data

A large volume of data was collected in these experiments that has to be processed before it can be further analyzed. Each dataset comprised 1000 snapshots, where these corresponded to frames from the aqueous droplets, the continuous oil phase, and the interfacial region between the oil and water. To obtain a signal from the nanoparticles alone, it was, therefore, necessary to isolate the frames from the aqueous droplets and then subtract the background arising from scattering from the capillary and the solution.

3.2.1 Creation of a Dataset of Droplet Frames

An example of the SAXS and WAXS data recorded over four consecutive frames is presented in Figure 4. This highlights the differences in scattering from the oil and aqueous phases, and the necessity to discard the unwanted frames before further analysis. The WAXS patterns collected from the droplets, the interface region, and the oil were each distinctive and can therefore be used to build a selection criterion that can automatically identify the origin of each frame.

While the WAXS pattern of an oil or interface frame exhibited a maximum intensity at a scattering vector of 1.2Å^{-1}, a droplet frame instead presented a broader "bump" around 1.5Å^{-1}. Comparison of the scattered intensities at 1.5Å^{-1} and 1.2Å^{-1} therefore, enabled the frames to be sorted. Let us define the selection criterion as R:

$$R = \frac{I(q = 1.5\text{Å}^{-1})}{I(q = 1.2\text{Å}^{-1})} \qquad \text{Eq.2}$$

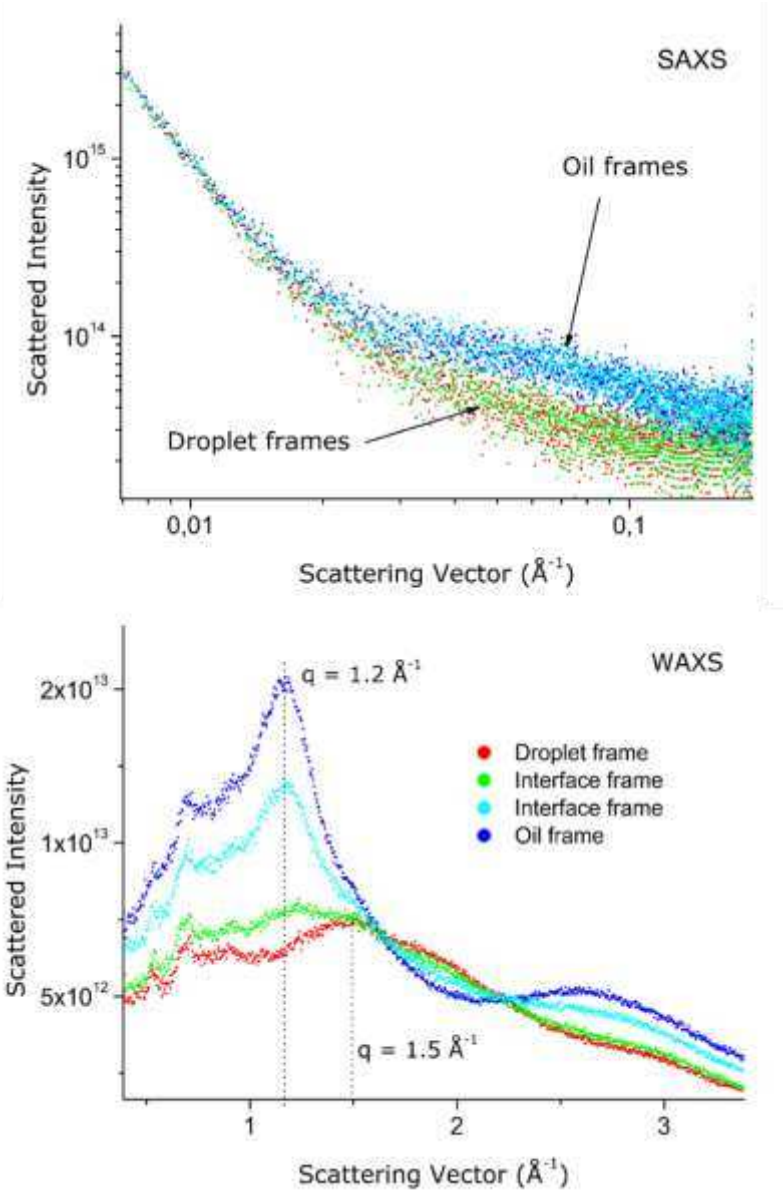

Figure 4. SAXS and WAXS intensities as a function of scattering vector for four consecutive frames in a dataset corresponding to continuous generation of droplets in oil. Two different kinds of frames appeared, with an average higher signal for the oil in SAXS and different structural features in WAXS.

For a given frame, if the value of R is greater than 1, the intensity at 1.5Å^{-1} is higher than that at 1.2Å^{-1}, meaning that this is an oil or an interface frame. In contrast, if R is less than 1, no maximum is observed at 1.5Å^{-1}, and the frame derived from a droplet. The application of this

criterion to an entire dataset consisting of 1000 consecutive frames is shown in **Error! Reference source not found.**a. The high magnification view highlights the stability of the droplet generation as well as the robustness of the selection criterion. A Python script was written to open all of the frames from a dataset, sort them according to this parameter, and remove the oil and interface frames. This offers a simple and rapid means of creating a new dataset comprising the droplet frames alone that can then be used for further analysis.

3.2.2 Identification of Nanoparticle-Rich Frames and Background Subtraction

After generating a dataset containing droplet frames only, it was necessary to combine these frames to generate a representative signal from a large array of droplets, and then to subtract the background corresponding to scattering from the capillary, solution, and surrounding air. These two steps would be straightforward if the droplets were all completely homogeneous. However, our experiments demonstrate that the nanoparticles are not uniformly dispersed throughout the droplets. An average of five frames was recorded from each droplet, of which the first two usually corresponded to aqueous solution only, and the last two derived from the nanoparticles. At least one intermediate frame corresponding to low-density nanoparticles was usually recorded from the middle of a droplet. The nanoparticles therefore accumulate at the back of the droplets due to their motion. This is illustrated in **Error! Reference source not found.**b, which shows the consecutive SAXS frames recorded from a single droplet.

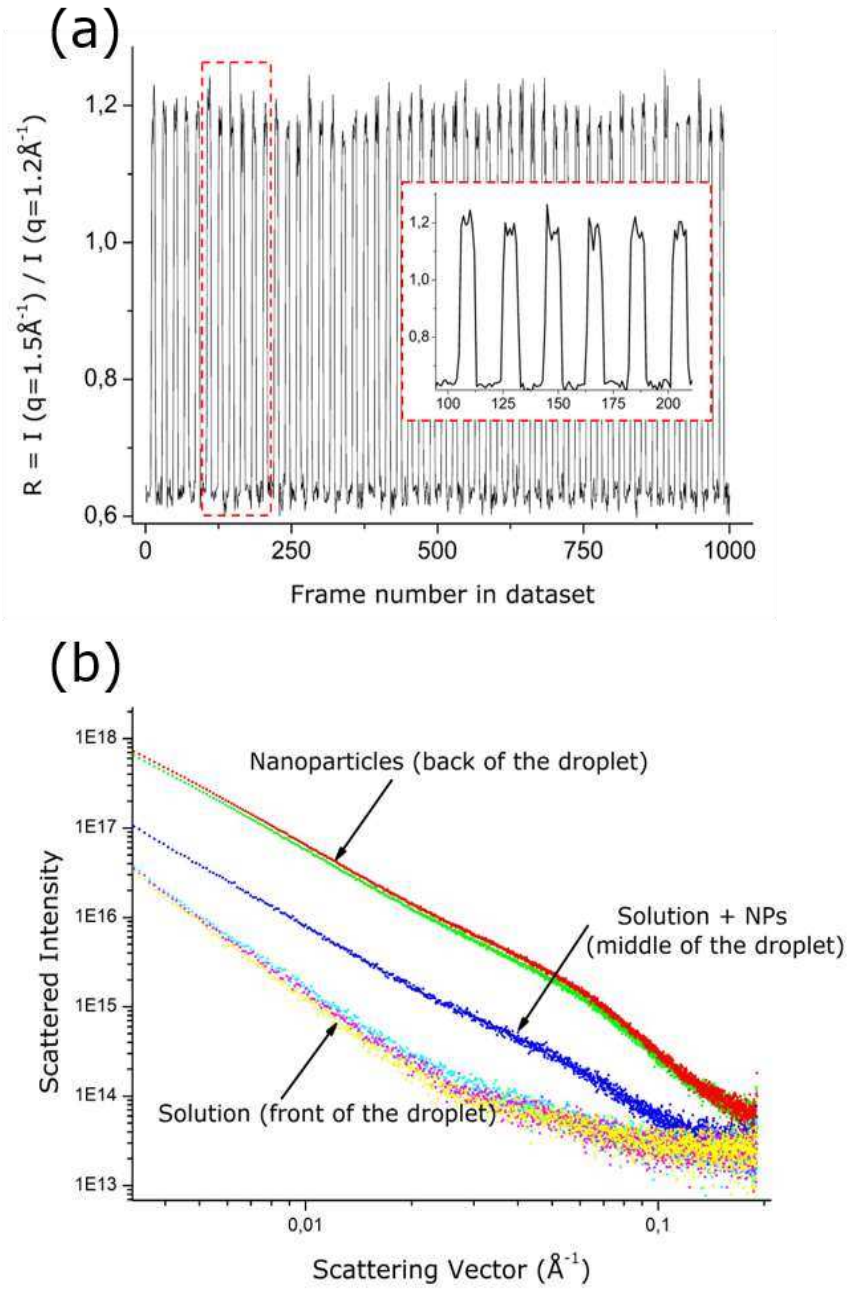

Figure 5. (a) Evolution of the selection criterion as a function of the frame number for an entire dataset derived from flowing droplets. The magnified inset demonstrates the stability of the droplet generation and the robustness of this parameter. (b) Consecutive SAXS frames within a dataset of flowing droplets. Three kinds of frames are obtained corresponding to solution only, nanoparticles-rich volume, or a low density of nanoparticles.

As the focus of this work is on the evolution of the magnetite nanoparticles, only the frames with the highest intensity are of interest. Assuming that the background contributions were identical in all droplet frames, the signal from the nanoparticles can be isolated by a frame-to-frame subtraction of the "empty" droplet frames from the "nanoparticle" frames. A Python script was once again written to automate this process, where it averaged the highest intensity frames, then the lowest intensity frames, and subtracted one from the other, delivering a scattering pattern from the nanoparticles alone. This sophisticated approach is significantly faster and delivers a much more reliable background subtraction than standard approaches in which a background would be obtained by operating the device with "empty" aqueous droplets. The entire experiment would then have to be stopped and repeated with the nanoparticle synthesis, leading to potential changes of the position of the device in the beam, and solution composition.

3.3 Collection of Time-Resolved Data

In these experiments, devices were employed in which seven different capillaries were positioned along the serpentine channel, giving different reaction times of between 10 and 130 sec (Table 1). These times were fine-tuned by adjusting the flow-rate. Three datasets comprising 1000 snapshots were recorded for each capillary, and the frames were processed as described above. This yielded the seven time-resolved SAXS and WAXS patterns for the formation of magnetite nanoparticles that are presented in **Error! Reference source not found.**. The SAXS evolution presented a Guinier plateau with an overall increase in the scattered intensity as a function of time and a slope that is more pronounced at medium scattering angles. These features are discussed in Section 3.4. The WAXS signal appears quite

flat at early times (30 sec), with diffraction peaks emerging after 50 sec and being quite pronounced by 90 sec.

Capillary	1	2	3	4	5	6	7
Time (sec)	10	30	50	70	90	110	130

Table 1. Time scales investigated during magnetite synthesis in the microfluidic device.

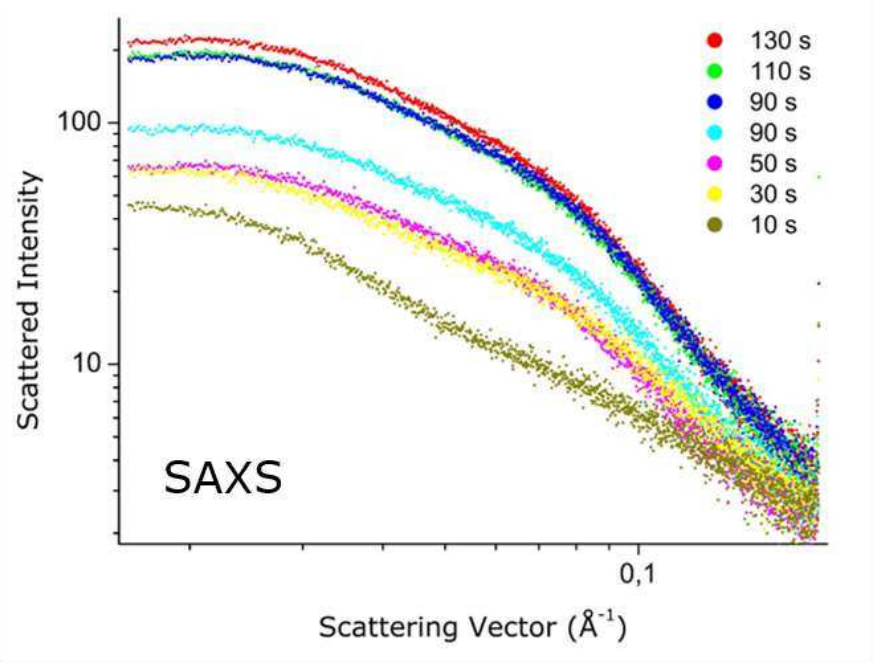

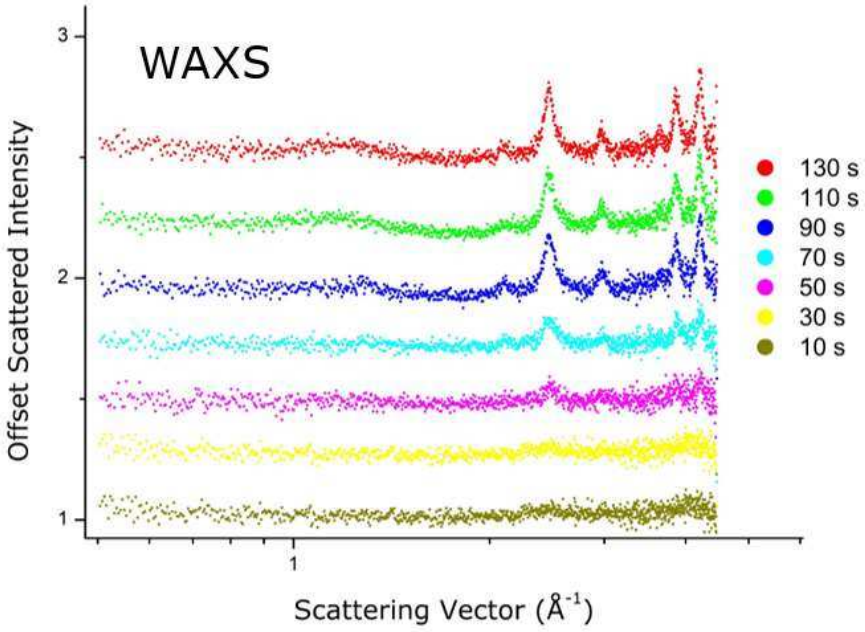

Figure 6. Time-resolved SAXS and WAXS patterns obtained on-chip during magnetite synthesis. The WAXS curves have been offset for clarity.

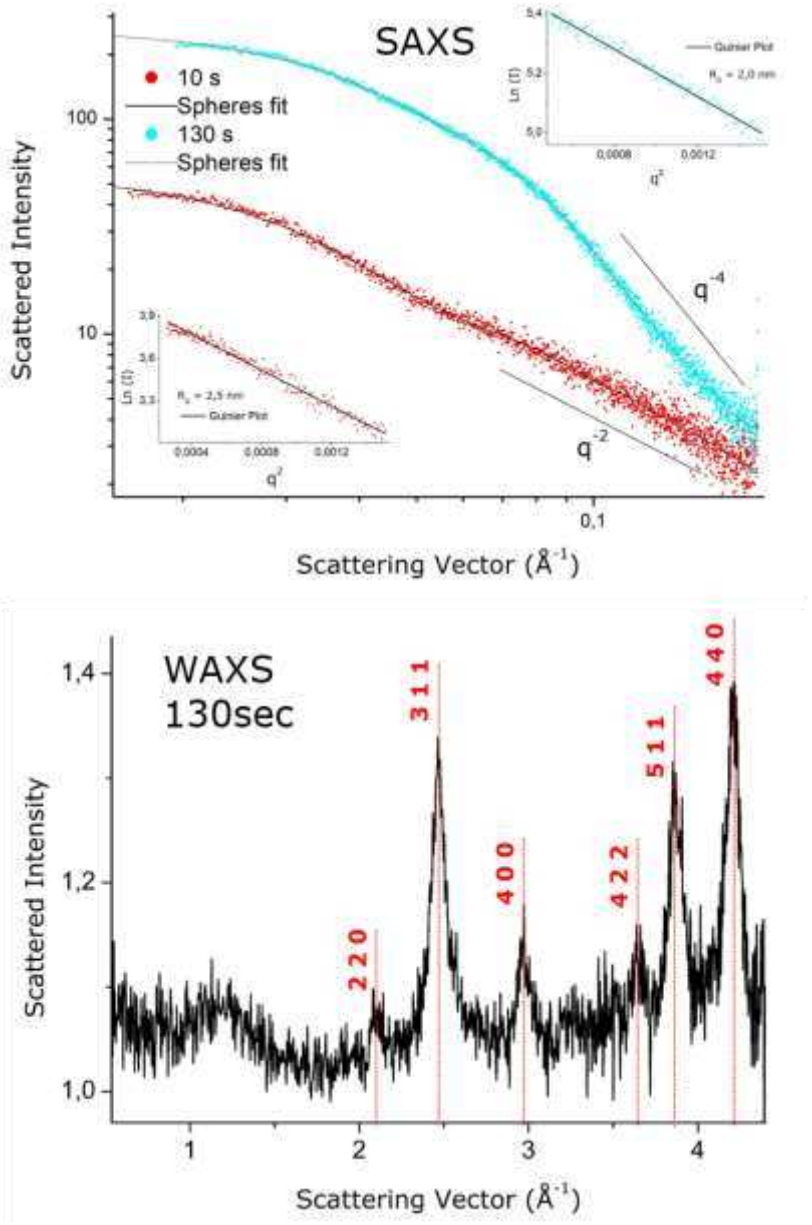

Figure 7. (a) Fitting of the experimental SAXS data for reaction times of 10 s and 130 s with a narrowly dispersed sphere model. The Guinier plot shown in the inset gives the radius of gyration of these particles. (b) The WAXS peaks obtained after 130 sec correspond to magnetite/ maghemite.

3.4 Modelling of SAXS and WAXS Data

In order to obtain structural information including the size of the nanoparticles and their structures, the time-resolved SAXS data were modeled with the ATSAS package software.[54] All of the scattering patterns were successfully modeled with a narrowly dispersed sphere model around the average radius (

a). Additional fitting of these data was also done with the software SASView, which gave similar results.

Finally, information about the structure of the nanoparticles was obtained from the time-resolved WAXS patterns (**Error! Reference source not found.**b). No diffraction peaks were observed at early times (10-30 sec) demonstrating that the precipitates were non-crystalline, or not enough crystalline material was present to diffract significantly. Diffraction peaks corresponding to magnetite developed at time > 50 sec (

b). This combined SAXS/WAXS study, therefore, shows that the precipitation of magnetite began with the presence of mostly amorphous material which later evolves to well-defined crystalline nanoparticles. This mechanism is in agreement with the TEM observation previously reported in this work.

This mechanism of magnetite formation is also in good agreement with recent observations reported in the literature with similar experimental conditions at room temperature,[56] underlining the effectiveness of our microfluidic synthesis and data analysis approach.

Magnetite is rapidly formed when base is added to an oxygen-free solution of 2:1 Fe^{3+}/ Fe^{2+} to give a pH of 8 to 14,[57] where the size of the particles is determined by the pH and the ionic strength.[58] Baumgartner et al. observed that this is preceded by the formation of amorphous iron oxy(hydroxide) nanoparticles that aggregate to form fractal assemblies in Cryo-TEM studies. Nuclei of crystalline magnetite then nucleate and grow within this amorphous phase rather than by a dissolution/ reprecipitation mechanism.[46] In contrast, only magnetite was detected at the earliest analysis time of 5s in a SAXS/WAXS study of precipitation in a flow system at 60°C.[51] As the reaction proceeds more rapidly at this elevated temperature, analysis at earlier times would be required to determine whether iron oxy(hydroxide) nanoparticles still form under these conditions, or whether magnetite precipitates directly. Such early times can be readily accessed using microfluidic devices of the type described here.

Conclusions

A segmented-flow microfluidic device was designed and built to synthesize magnetite nanoparticles in well-defined environments *on-chip* such that their crystallization pathway can be studied *in situ* using SAXS/ WAXS. While this approach offers many advantages for studying crystallization processes, extracting and processing the data from heterogeneous flow systems can be laborious. Here, we demonstrate how the simultaneous acquisition of SAXS and WAXS data from these flowing droplets can be used to establish a straightforward and versatile approach for processing the data. WAXS patterns were used to sort the acquired frames based on a criterion describing the unique structural features of the WAXS patterns recorded from the oil and aqueous droplets. SAXS patterns were subsequently used to sort the frames deriving from the aqueous droplets, where analysis of the frames in sequence demonstrates that the nanoparticles are concentrated at the back of the droplets due to their

motion such that the front is free of nanoparticles. The frame recorded at the front of a droplet can therefore be used to achieve an ideal background subtraction for the SAXS data recorded from the nanoparticles at the rear of the droplet. Automating this *frame-by-frame* subtraction strategy delivers rapid, high-quality processing of SAXS and WAXS data from segmented flow systems. Data analysis can then be carried out using standard methods, giving information about the crystallization pathway. With microfluidic systems now becoming mainstream, this data-processing method will ensure that segmented-flow microfluidic systems can be readily employed to study processes such as crystallization, where these environments offer highly-reproducible reaction environments and give access to very short reaction times with excellent time resolution.

Conflicts of interest

There are no conflicts to declare.

Acknowledgements

This work was supported by a UK Engineering and Physical Sciences Research Council (EPSRC) Platform Grant (EP/N002423/1) and received funding from the European Research Council (ERC) under the project DYNAMIN - DLV-788968. The authors acknowledge Diamond Light Source for time on beamline ID22 under proposal SM23902. We thank beamline scientists Andy Smith and Tim Snow for assistance.

References

1 L. A. Feigin and D. I. Svergun, *Structure Analysis by Small-Angle X-Ray and Neutron Scattering*, Springer US, Boston, MA, 1987.

2 O. Glatter and O. Kratky, *Small angle x-ray scattering*, Academic Press, London, 1982.

3 A. Guinier, G. Fournet and K. L. Yudowitch, *Small-angle scattering of X-rays*, Wiley, New-York, 1955.

4 A. Ducruix, J. P. Guilloteau, M. Riès-Kautt and A. Tardieu, *J. Cryst. Growth*, 1996, **168**, 28–39.

5 H. Fischer, O. Neto, M. De, H. B. Napolitano, I. Polikarpov and A. F. Craievich, *J. Appl. Crystallogr.*, 2010, **43**, 101–109.

6 H. D. T. Mertens and D. I. Svergun, *J. Struct. Biol.*, 2010, **172**, 128–141.

7 H. Durchschlag, P. Zipper, R. Wilfing and G. Purr, *J. Appl. Crystallogr.*, 1991, **24**, 822–831.

8 T. Uzawa, T. Kimura, K. Ishimori, I. Morishima, T. Matsui, M. Ikeda-Saito, S. Takahashi, S. Akiyama and T. Fujisawa, *J. Mol. Biol.*, 2006, **357**, 997–1008.

9 R. Stehle, G. Goerigk, D. Wallacher, M. Ballauff and S. Seiffert, *Lab. Chip*, 2013, **13**, 1529–1537.

10 1D. Pontoni, T. Narayanan and A. R. Rennie, in *Trends in Colloid and Interface Science XVI*, eds. M. Miguel and H. D. Burrows, Springer, Berlin, Heidelberg, 2004, 227–230.

11 1J. Becker, M. Bremholm, C. Tyrsted, B. Pauw, K. M. Ø. Jensen, J. Eltzholt, M. Christensen and B. B. Iversen, *J. Appl. Crystallogr.*, 2010, **43**, 729–736.

12 1X. Chen, J. Wang, R. Pan, S. Roth and S. Förster, *J. Phys. Chem. C*, 2021, **125**, 1087–1095.

13 X. Chen, J. Schröder, S. Hauschild, S. Rosenfeldt, M. Dulle and S. Förster, *Langmuir*, 2015, **31**, 11678–11691.

14 B. Ingham, *Crystallogr. Rev.*, 2015, **21**, 229–303.

15 B. Abécassis, F. Testard, O. Spalla and P. Barboux, *Nano Lett.*, 2007, **7**, 1723–1727.

16 F. Meneau, G. Sankar, N. Morgante, S. Cristol, C. R. A. Catlow, J. M. Thomas and G. N. Greaves, *Nucl. Instrum. Methods Phys. Res. Sect. B Beam Interact. Mater. At.*, 2003, **199**, 499–503.

17 P. R. A. F. Garcia, O. Prymak, V. Grasmik, K. Pappert, W. Wlysses, L. Otubo, M. Epple and C. L. P. Oliveira, *Nanoscale Adv.*, 2020, **2**, 225–238.

18 J. B. Hopkins and R. E. Thorne, *J. Appl. Crystallogr.*, 2016, **49**, 880–890.

19 A. Ghazal, J. P. Lafleur, K. Mortensen, J. P. Kutter, L. Arleth and G. V. Jensen, *Lab. Chip*, 2016, **16**, 4263–4295.

20 N. Pham, D. Radajewski, A. Round, M. Brennich, P. Pernot, B. Biscans, F. Bonneté and S. Teychené, *Anal. Chem.*, 2017, **89**, 2282–2287.

21 I. Rodríguez-Ruiz, D. Radajewski, S. Charton, N. Phamvan, M. Brennich, P. Pernot, F. Bonneté and S. Teychené, *Sensors*, 2017, **17**, 1266.

22 I. Rodríguez-Ruiz, S. Charton, D. Radajewski, T. Bizien and S. Teychené, *CrystEngComm*, 2018, **20**, 3302–3307.

23 M. A. Levenstein, C. Anduix-Canto, Y. Kim, M. A. Holden, C. González Niño, D. C. Green, S. E. Foster, A. N. Kulak, L. Govada, N. E. Chayen, S. J. Day, C. C. Tang, B. Weinhausen, M. Burghammer, N. Kapur and F. C. Meldrum, *Adv. Funct. Mater*, 2019, **29**, 1808172.

24 R. Graceffa, R. P. Nobrega, R. A. Barrea, S. V. Kathuria, S. Chakravarthy, O. Bilsel and T. C. Irving, *J. Synchrotron Radiat.*, 2013, **20**, 820–825.

25 D. S. Khvostichenko, E. Kondrashkina, S. L. Perry, A. S. Pawate, K. Brister and P. J. A. Kenis, *The Analyst*, 2013, **138**, 5384–5395.

26 H. P. Martin, N. J. Brooks, J. M. Seddon, N. J. Terrill, P. F. Luckham, A. J. Kowalski and J. T. Cabral, *J. Phys. Conf. Ser.*, 2010, **247**, 012050.

27 M. E. Brennich, J.-F. Nolting, C. Dammann, B. Nöding, S. Bauch, H. Herrmann, T. Pfohl and S. Köster, *Lab. Chip*, 2011, **11**, 708–716.

28 M. Herbst, E. Hofmann and S. Förster, *Langmuir*, 2019, **35**, 11702–11709.

29 A. M. Karim, N. Al Hasan, S. Ivanov, S. Siefert, R. T. Kelly, N. G. Hallfors, A. Benavidez, L. Kovarik, A. Jenkins, R. E. Winans and A. K. Datye, *J. Phys. Chem. C*, 2015, **119**, 13257–13267.

30 J. Polte, R. Erler, A. F. Thünemann, S. Sokolov, T. T. Ahner, K. Rademann, F. Emmerling and R. Kraehnert, *ACS Nano*, 2010, **4**, 1076–1082.

31 M. A. Levenstein, Y.-Y. Kim, L. Hunter, C. Anduix-Canto, C. González Niño, S. J. Day, S. Li, W. J. Marchant, P. A. Lee, C. C. Tang, M. Burghammer, F. C. Meldrum and N. Kapur, *Lab. Chip*, 2020, **20**, 2954–2964.

32 S. Sohrabi, N. kassir and M. Keshavarz Moraveji, *RSC Adv.*, 2020, **10**, 27560–27574.

33 B. Zheng, L. S. Roach and R. F. Ismagilov, *J. Am. Chem. Soc.*, 2003, **125**, 11170–11171.

34 L. Li, D. Mustafi, Q. Fu, V. Tereshko, D. L. Chen, J. D. Tice and R. F. Ismagilov, *Proc. Natl. Acad. Sci.*, 2006, **103**, 19243–19248.

35 Š. Selimović, Y. Jia and S. Fraden, *Cryst. Growth Des.*, 2009, **9**, 1806–1810.

36 S. Teychené and B. Biscans, *Chem. Eng. Sci.*, 2012, **77**, 242–248.

37 P. Laval, A. Crombez and J.-B. Salmon, *Langmuir*, 2009, **25**, 1836–1841.

38 Y. Vitry, S. Teychené, S. Charton, F. Lamadie and B. Biscans, *Chem. Eng. Sci.*, 2015, **133**, 54–61.

39 L.-H. Hung, K. M. Choi, W.-Y. Tseng, Y.-C. Tan, K. J. Shea and A. P. Lee, *Lab. Chip*, 2006, **6**, 174.

40 I. Shestopalov, J. D. Tice and R. F. Ismagilov, *Lab. Chip*, 2004, **4**, 316.

41 J. Wang, Y. Li, X. Wang, J. Wang, H. Tian, P. Zhao, Y. Tian, Y. Gu, L. Wang and C. Wang, *Micromachines*, 2017, **8**, 22.

42 L. Xu, J. Peng, M. Yan, D. Zhang and A. Q. Shen, *Chem. Eng. Process. Process Intensif.*, 2016, **102**, 186–193.

43 A. Otten, S. Köster, B. Struth, A. Snigirev and T. Pfohl, *J. Synchrotron Radiat.*, 2005, **12**, 745–750.

44 R. Ramadan, S. I. El-Dek and M. M. Arman, *Appl. Phys. A*, 2020, **126**.

45 L. Blaney, Lehig Preserve, 2007, **15**, 33-81.

46 J. Baumgartner, A. Dey, P. H. H. Bomans, C. Le Coadou, P. Fratzl, N. A. J. M. Sommerdijk and D. Faivre, *Nat. Mater.*, 2013, **12**, 310–314.

47 D. Faivre and D. Schüler, *Chem. Rev.*, 2008, **108**, 4875–4898.

48 K. Petcharoen and A. Sirivat, *Mater. Sci. Eng. B*, 2012, **177**, 421–427.

49 F. Yazdani and M. Seddigh, *Mater. Chem. Phys.*, 2016, **184**, 318–323.

50 S. Laurent, D. Forge, M. Port, A. Roch, C. Robic, L. Vander Elst and R. N. Muller, *Chem. Rev.*, 2008, **108**, 2064–2110.

51 M. O. Besenhard, A. P. LaGrow, A. Hodzic, M. Kriechbaum, L. Panariello, G. Bais, K. Loizou, S. Damilos, M. Margarida Cruz, N. T. K. Thanh and A. Gavriilidis, *Chem. Eng. J.*, 2020, **399**, 125740.

52 L. Frenz, A. El Harrak, M. Pauly, S. Bégin-Colin, A. D. Griffiths and J.-C. Baret, *Angew. Chem. Int. Ed.*, 2008, **47**, 6817–6820.

53 A. Folch, A. Ayon, O. Hurtado, M. A. Schmidt and M. Toner, *J. Biomech. Eng.*, 1999, **121**, 28–34.

54 K. Manalastas-Cantos, P. V. Konarev, N. R. Hajizadeh, A. G. Kikhney, M. V. Petoukhov, D. S. Molodenskiy, A. Panjkovich, H. D. T. Mertens, A. Gruzinov, C. Borges, C. M. Jeffries, D. I. Svergun and D. Franke, *J. Appl. Crystallogr.*, 2021, **54**, 343–355.

55 H. S. C. O'Neill and W. A. Dollase, *Phys. Chem. Miner.*, 1994, **20**, 541–555.

56 J. Baumgartner, R. K. Ramamoorthy, A. P. Freitas, M.-A. Neouze, M. Bennet, D. Faivre and D. Carriere, *Nano Lett.*, 2020, **20**, 5001–5007.

57 G. Mirabello, J. J. M. Lenders and N. A. J. M. Sommerdijk, *Chem. Soc. Rev.*, 2016, **45**, 5085–5106.

58 L. Vayssieres, C. Chanéac, E. Tronc and J. P. Jolivet, *J. Colloid Interface Sci.*, 1998, **205**, 205–212.